Monitoring Vegetation Condition using Microwave Remote Sensing: The Standardized Vegetation Optical Depth Index SVODI

Leander Moesinger[1], Ruxandra-Maria Zotta[1], Robin van der Schalie[2], Tracy Scanlon[1], Richard de Jeu[2], and Wouter Dorigo[1]

[1]Technische Universität Wien, Department of Geodesy and Geoinformation, Vienna, Austria
[2]VanderSat, Wilhelminastraat 43A, 2011 VK Haarlem, The Netherlands

Correspondence: Leander Moesinger (Leander.Moesinger@geo.tuwien.ac.at, vodca@geo.tuwien.ac.at), Wouter Dorigo
(Wouter.Dorigo@tuwien.ac.at)

Abstract. Vegetation conditions can be monitored on a global scale using remote sensing observations in various wavelength domains. In the microwave domain, data from various spaceborne microwave missions are available from the late 1970s onwards. From these observations, vegetation optical depth (VOD) can be estimated, which is an indicator of the total canopy water content and hence of above-ground biomass and its moisture state. Observations of VOD anomalies would thus complement

5 indicators based on visible and near-infrared observations, which are primarily an indicator of an ecosystem's photosynthetic activity.

Reliable long-term vegetation state monitoring needs to account for the varying number of available observations over time caused by changes in the satellite constellation. To overcome this, we introduce the Standardized Vegetation Optical Depth Index (SVODI), which is created by combining VOD estimates from multiple passive microwave sensors and frequencies.

10 Different frequencies are sensitive to different parts of the vegetation canopy. Thus, by combining them into a single index makes this index sensitive to deviations in any of the vegetation parts represented. SSM/I, TMI, AMSR-E, WindSat and AMSR2-derived C-, X- and Ku-band VOD are merged in a probabilistic manner resulting in a vegetation condition index spanning from 1987 to the present.

SVODI shows similar temporal patterns as the well-established optical vegetation health index (VHI) derived from optical

15 and thermal data. In regions where water availability is the main control of vegetation growth, SVODI also shows similar temporal patterns as the meteorological drought index scPDSI and soil moisture anomalies from ERA-land. Temporal SVODI patterns relate to the climate oscillation indices SOI and DMI in the relevant regions. It is further shown that anomalies occur in VHI and soil moisture anomalies before they occur in SVODI.

The results demonstrate both the potential of VOD to monitor the vegetation condition supplementing existing optical indices.

20 It comes with the advantages and disadvantages inherent to passive microwave remote sensing, such as being less susceptible to cloud coverage and solar illumination but at the cost of a lower spatial resolution. The index generation is not specific to VOD and could therefore find applications in other fields.

SVODI is open-access and available at xy [once the paper is through review].

1 Introduction

25 Monitoring vegetation conditions by remote sensing is important for a variety of purposes, such as agricultural yield prediction (Petersen, 2018; Crocetti et al., 2020), forestry (Pause et al., 2016), fire ecology (Szpakowski and Jensen, 2019), and to track long-term ecosystem changes (Vogelmann et al., 2012). On a global scale, observing vegetation conditions from space allows for cost-effective, long-term, and spatially consistent analyses.

30 Numerous variables and metrics have been developed to monitor vegetation conditions from space-borne observations. Some use the spectral or radiometric information directly to create a feature related to the vegetation. This includes features such as the Normalized Difference Vegetation Index (NDVI), which is widely used as a measure of live green vegetation (Huang et al., 2021; Tucker et al., 2005), or the cross-polarization ratio (CR) which is related to polarization changes of active microwaves caused by vegetation structure and moisture content (Vreugdenhil et al., 2020).

35 Often, radiometric information is translated into biogeophysical or -chemical variables such as the Leaf Area Index (LAI) or the fraction of absorbed photosynthetic radiation (Dorigo et al., 2007). An ecosystem's condition can also be observed through its response to stress, e.g., by measuring changes in land surface temperature (Kogan, 1990) or evaporation (Martens et al., 2017).

All these features have in common that they show some aspect of the vegetation at a given time and location.

40

To assess whether the state of the vegetation is unusual at a given time and location, it is usually compared against the expected value at that time of year, derived from long-term observations. There there are multiple ways to do this. The most straightforward way is to calculate anomalies by subtracting the multiyear seasonal average from the observation. This allows one to directly see whether an observation is higher or lower than usual. The drawback of such raw anomalies is that their

45 magnitude depends on the average conditions at a given location. Therefore, the anomalies between different locations cannot be compared against each other and it requires expert-knowledge to know whether an anomaly of a certain magnitude is a very strong outlier or a minor deviation (Katz and Glantz, 1986).

This can be solved by expressing deviations from normal conditions as an index. While anomalies show deviations as absolute differences to some mean, indices show the likelihood of observing a deviation of a certain magnitude. Indices are easier to

50 interpret, as they follow a well-defined distribution which allows one to discern quickly whether a value is relatively high or low.Some well-known example indices are the Vegetation Condition Index (VCI, computed from NDVI, (Kogan, 1990, 1997, 2001)), the Temperature Condition Index (TCI, computed from observations in the thermal domain (Kogan, 1990, 1997, 2001)), and the Standardized Precipitation Index (SPI, from precipitation estimates(Thomas B. McKee and Kleist, 1993)).

55 Over the past four decades, various platforms carrying multi-frequency microwave radiometers have been orbiting the earth. From these observations it is possible to derive the Vegetation Optical Depth (VOD), which describes the attenuation of microwave radiation by vegetation (Jackson and Schmugge, 1991; Meesters et al., 2005). The higher the vegetation water

content and the shorter the wavelength, the more the vegetation attenuates the radiation (Jackson and Schmugge, 1991; Owe et al., 2008). Each frequency band is sensitive to slightly different parts of the vegetation, with short-wavelengths such as
60 measured by the Ku-band being mostly related to the canopy top and leaves, while longer wavelengths are also sensitive to the woody vegetation parts (Owe et al., 2008; Rodríguez-Pérez et al., 2018). Compared to indices derived from optical data, VOD saturates less quickly for dense canopies and is therefore more sensitive to fluctuations in densely vegetated areas (Liu et al., 2015; Frappart et al., 2020). Among many other things, VOD has been used to analyze the vegetation's response to droughts in the Amazonian tropics (Liu et al., 2018) and in the Pannonian Basin (Crocetti et al., 2020) and to determine deforestation in
65 the tropics (van Marle et al., 2015).

Long-term VOD datasets, such as VODCA (Moesinger et al., 2020) or the dataset presented by (Liu et al., 2015), allow for monitoring vegetation conditions over decadal timescales. It might seem trivial to create an index from any of these datasets by calculating the seasonal anomalies and standardizing them. However, these datasets are based on averaging all available VOD values from different sensors. This causes the merged data to be heteroscedastic, where periods with fewer observations are
70 noisier than periods with more observations. High noise levels increase the probability of a value to be extreme, and therefore extreme values are more likely to occur in periods with few observations and high noise. This hampers comparisons of extreme events over longer time periods.

To solve this issue, the Standardized VOD Index (SVODI) is proposed, which uses a probabilistic merging method to generate a long-term dataset for global vegetation condition monitoring based on VOD. After a technical evaluation, its relationship to
75 other vegetation-related indices is explored. This assures that SVODI behaves reasonably in the case of an event affecting the vegetation and to give insight into how it differs from the currently used indices for vegetation condition monitoring.

2 Data

2.1 Vegetation Optical Depth data sets

2.1.1 The land-parameter retrieval model (LPRM)

80 VOD estimates from various microwave radiometers and frequencies have been obtained with LPRM v6.0 (van der Schalie et al., 2017; Owe et al., 2008; Meesters et al., 2005), which is a forward radiative transfer model based on the work of Mo et al. (1982). It simulates the top-of-atmosphere brightness temperature for a wide range of surface conditions. It retrieves soil moisture and VOD analytically using polarized microwave data and Ka-band surface temperature estimations (Holmes et al., 2009) without relying on external information on the vegetation. Since the surface temperature estimation is more challenging
85 during the day than during the night (Owe et al., 2008), only nighttime VOD observations are used. This choice is in line with other studies using LPRM data (Dorigo et al., 2017; Moesinger et al., 2020).

2.1.2 Sensor specifications

For this study, the exact same data as for VODCA (Moesinger et al., 2020) are used, namely VOD data derived from the
radiometers SSM/I, TMI, AMSR-E, WindSat and AMSR2. An overview of the specifications can be found in table 1. All
sensors but TMI have a sun-synchronous circular orbit, resulting in global coverage.

AMSR-E, the Advanced Microwave Scanning Radiometer onboard Aqua, is used from 2002 to 2011. The VOD retrieved
from C-, X-, and Ku-band are used which have a spatial footprint of 75×43 km, 51×29 km and 27×16 km respectively. Only
the descending overpass is used, which passes the equator 1:30 AM (Knowles et al., 2006; Kawanishi et al., 2003)

AMSR2, the Advanced Microwave Scanning Radiometer 2 onboard GCOM-W1, is used from June 2012 onwards. It is the
follow-up to AMSR-E and as such is very similar, but with slightly higher spatial resolution of 62×35 km, 42×24 km and
22×14 for the C-, X-, and Ku-band respectively. Another improvement is the addition of a second C-band (7.3 Ghz) that
can be used in case Radio-Frequency Interference (RFI) is affecting the primary C-band (6.9 GHz) (Meier et al., 2018). For
C- and X-band, all retrieved daytime VOD is used. For Ku-band, preliminary analysis revealed that the VOD retrievals after
2017-08-01 abruptly drop globally, possible due to a calibration issue. While the exact reason is not known, the data is deemed
unreliable and not used after that date.

SSMI, The Special Sensor Microwave Imager, F08, F11 and F13 onboard DMSP satellites are used for a total time span of
1987 to 2015. VOD retrieved from Ku-band with a resolution of 69×43 km is used (Wentz, 1997).

TMI, the TRMM Microwave Imager onboard TRMM, is used from 1997 to 2015. The VOD retrieved from X- and Ku-band
are used. Flying in a non-near-polar orbit, it only covered the area 35 degrees N/S until 2001, when a boost in altitude increased
it to about 37 degrees N/S. This also decreased the spatial resolution of X-band from 63×37 km to 72×43 km and of Ku-band
from 30×18 km to 35×21 km (Kummerow et al., 1998).

WindSat onboard Coriolis observes X- and Ku-band with a spatial resolution of 39×71 km, 25×38 km and 16×27 km
respectively and the retrieved VOD values from 2003 to 2012 are used (Gaiser et al., 2004). WindSat is still in orbit and func-
tional, but no access to data past 2012 was given.

2.2 Auxiliary data

Multiple auxiliary datasets are used to evaluate SVODI. Most of these datasets do not follow a standard normal distribution,
either by design or because the pre-processing (regridding and temporal resampling) changed their distribution. To facilitate
the comparison of all datasets, they are standardized using a basic Z-score normalization:

$$x_{standardized} = \frac{(x - \mu_x)}{\sigma_x} \tag{1}$$

where $x_{standardized}$ is the standardized data, x is the original data and μ_x and σ_x are its mean and standard deviation, respectively. This ensures that all data sets for the comparison have a mean of 0 and a standard deviation of 1.

2.2.1 Vegetation Health Index, Vegetation Condition Index, and Temperature Condition Index

The Vegetation Health Index (VHI) (Kogan, 1990, 1997, 2001) is derived from optical and thermal observations. The general
125 concept is to combine water and temperature stress indices into a combined vegetation health index (Kogan, 2001). As such, the VHI is a weighted average of the Vegetation Condition Index (VCI) and Temperature Condition Index (TCI),

$$VHI = \alpha VCI + (1 - \alpha)TCI \tag{2}$$

where the weight α is traditionally set to 0.5 (Kogan, 1997). The VCI is derived from NDVI, and as such contains information about the greenness of the vegetation:

130 $$VCI = 100 \cdot \frac{NDVI - NDVI_{min}}{NDVI_{max} - NDVI_{min}} \tag{3}$$

where $NDVI$, $NDVI_{min}$ and $NDVI_{max}$ are the smoothed weekly NDVI, its multiyear minimum and maximum NDVI, respectively. The VCI was used successfully for drought monitoring and assessing vegetation conditions (Kogan, 1997) and in the VHI is assumed to account for water stress.

The TCI is defined similarly, but based on land surface temperature (LST),

135 $$TCI = 100 \cdot \frac{LST_{max} - LST}{LST_{max} - LST_{min}} \tag{4}$$

where LST, LST_{min} and LST_{max} are the smoothed weekly land surface temperature, its multiyear minimum, and its multiyear maximum, respectively. The TCI increased the accuracy of drought monitoring by accounting for temperature stress and was used to analyze the role of temperature in droughts (Kogan, 1997). By combining it with the VCI both water and temperature stress are accounted for.

140

VHI, VCI and TCI derived from AVHRR NDVI (Tucker et al., 2005) and the thermal channel 4, respectively, are used. The data are available at https://www.star.nesdis.noaa.gov. The data were downsampled from the original 4 km resolution to match our quarter degree grid, and standardized using equation 1.

145 2.2.2 Self-calibrating Palmer Drought Severity Index

The self-calibrating Palmer Drought Severity Index (scPDSI) (Wells et al., 2004; Van Der Schrier et al., 2013; Aldred et al., 2021) is a widely used index to track meteorological, agricultural, and hydrological aspects of drought. It is used to analyse the relation between SVODI and meteorological droughts. One of the main drawbacks of the original PDSI (Palmer, 1965) was its lack of spatial comparability due to fixed weights and factors, which was remedied in the scPDSI by adjusting them to the
150 local climate. The scPDSI models the soil moisture using bucket model involving evaporation, recharge, runoff, loss and their

complementary potential values. This gives a measure of how extreme the water conditions are at a certain time and place, which is useful for monitoring water stress. The scPDSI data is available at https://crudata.uea.ac.uk/cru/data/drought/.

2.2.3 ERA5-Land

155 ERA5-Land is a reanalysis of the global atmosphere, land surface and ocean waves since 1950 (Muñoz-Sabater et al., 2021; Hersbach et al., 2020). ERA5-Land models a plethora of land variables on a sub-daily temporal resolution. Of interest for our study is the modeled soil moisture at different depths, which is used assess the relation between SVODI and soil moisture at different depths (section 4.2.2). ERA5-Land is available from the Climate Data Store at https://doi.org/10.24381/cds.e2161bac

2.2.4 SOI and DMI

160 The Southern Oscillation Index (SOI) (Allan et al., 1991; Allan, 1998) and Dipole Mode Index (DMI) (Saji et al., 1999; Saji and Yamagata, 2003) are useful to monitor large-scale climate oscillations in the tropics. The SOI is derived from the sea-level atmospheric pressure difference between Tahiti and Darwin, while the DMI is calculated from the difference in sea surface temperature anomaly between the west and south-eastern tropical Indian Ocean. Among other things, both of them are are linked to precipitation anomalies in Australia and North-Eastern Africa, regions where the vegetation is water-limited and

165 where they are therefore also expected to be linked to the vegetation condition (Hashimoto et al., 2019; Martens et al., 2018).

Both are available at NOAA, at https://psl.noaa.gov/gcos_wgsp/Timeseries/SOI and https://psl.noaa.gov/gcos_wgsp/Timeseries/DMI, respectively.

3 Methods

3.1 SVODI calculation

170

SVODI is computed from C-, X- and Ku-band VOD from multiple sensors. It is assumed that all sensors and bands are equally fit as an indicator of the vegetation condition but show different aspects of it. Ku-band is mostly sensitive to surface canopy leaves, while longer wavelengths also are affected by the woody part (Owe et al., 2008; Rodríguez-Pérez et al., 2018). Still, the seasonal VOD anomalies of the three bands correlate strongly with each other (figure 1) as established in previous studies

175 (Moesinger et al., 2020), which suggests that they behave similarly in case of a vegetation disturbance. To maximize the information contained in a microwave-based vegetation condition index, it makes sense to combine the information contained in all bands. Also, the high number of observations per day available due to the many sensors and bands is expected to yield an index robust to noise. Additionally, none of the bands span the whole time period (VOD-C 2002 to present, VOD-X 1997 to present, VOD-Ku 1987 to 2017), so by merging them the longest possible time span is achieved.

3.1.1 Theory

Previous multi-variate indices (Hao and AghaKouchak, 2013; Guo et al., 2019) have been constructed by first fitting a multivariate distribution with cumulative joint probability $P(X_1 \leq x_1, ..., X_n \leq x_n) = p_{combined}$ to n individual indexes $X_i, i \in 1, ..., n$. Then, the $p_{combined}$ of each observation $(x_1, ..., x_n)$ is transformed to the index by applying the standard normal percent point function (PPF, the inverse of the cumulative distribution function) to it.

But there is an issue with this approach: $p_{combined}$ is not uniformly distributed between 0 and 1. Instead, it has a bias towards low values. This is illustrated for a theoretical bi-variate case in figure 2: If some x_1, x_2 pairs are drawn and calculate p for them, the distribution of $p_{combined}$ is clearly not uniformly distributed. This causes the final index to have a negative bias. For example, consider the case $x_1 = x_2 = 0$, marked with red lines in figure 2. Instinctively, since both input indexes show usual conditions, one would expect that the merged index should also show usual conditions. However, as seen in the figure, $P(X_1 \leq 0, X_2 \leq 0) < 0.50$, and therefore $PPF(p_{combined}) < 0$. Therefore, even if all input indices are 0, the merged index will be negative. For a higher number of concurrent indices used as input, this effect is even stronger. In general, this would lead to an index with much more extreme negative events than positive ones (figure 2, right).

The negative bias of multi-variate indices computed as above makes the index hard to interpret, as the resulting index is no longer normally distributed. Also, in case the individual indexes have data gaps, the expected mean depends on the available input indexes, leading to a higher expected value for periods where fewer sensors are available than for periods with more sensors available. This issue is solved by scaling $p_{combined}$ to a uniform distribution whose properties do not change depending on the number of available input indexes. Therefore SVODI has no bias and can also be calculated if not all input data sets are available.

3.1.2 Implementation

After some basic preprocessing (temporal resampling of swath data to daily values, masking invalid values, same as in (Moesinger et al., 2020)), the VOD values of each sensor and band, $VOD_{s,b}$ are transformed independently into standard normally distributed indexes using the following workflow, which is independently applied for each band:

Long-term VOD changes are related to biomass changes (Frappart et al., 2020). The input datasets are therefore linearly detrended to ensure that anomalies correspond to deviations in vegetation condition and not to long-term structural changes. Linear detrending might not be sufficient in areas experiencing rapid vegetation changes over a short time, but its simplicity guarantees that no deviations of interest are removed. Then, all VOD values of the respective band, VOD_b are scaled to the values of corresponding AMSR-E band to correct for bias between the different VOD_b using improved piece-wise linear CDF matching as described in Moesinger et al. (2020). In detail, SSMI, TMI and WindSat are matched to AMSR-E using temporally overlapping observations. AMSR2 does not have a temporal overlap with AMSRE, and therefore a direct matching using

overlapping observations is not possible. Instead, between 37 degrees North/South AMSR2 is matched to TMI observations
that were first scaled to AMSR-E. Beyond 37 degrees North/South, AMSR2 is directly matched to AMSR-E using the last two

215   years of AMSR-E and first two years of AMSR2 to determine the scaling parameters.

The scaled VOD values are standardized in the following way: For a day of the year ($\text{DOY}_i, i \in 1, 2, ..., 366$), all VOD_b
from 2002-07 to 2017-06 that are less than 16 days apart from DOY_i are used to build an empirical distribution. This window
size of 31 days was empirically chosen as a compromise between having enough values to build stable scaling parameters and

220   the values not being biased in respect to the window center due to the progressing seasonal VOD signal. The period July 2002
- June 2017 is chosen because all three frequency bands have observations during this period. Then, CDF scaling parameters
are calculated to transform the empirical distribution to a $N(0,1)$ distribution. Using these parameters, the VOD_b at DOY_i
are scaled. This is repeated for all DOYs and done independently for each band, resulting in individual indexes $X_{s,b}$ for each
$VOD_{s,b}$.

225   The indexes of the individual sensors and bands, $X_{s,b}$, are then joined by constructing a multivariate normal distribution
with a zero mean. As discussed before, if $P(X_1 \leq x_1, ..., X_n \leq x_n) = p_{combined}$, then $p_{combined}$ is not uniformly distributed
but is biased towards low values. Therefore, $p_{combined}$ is scaled to a uniform distribution. Technically this is done by draw-
ing random samples from P and constructing an empirical CDF CDF_P from them. $p_{combined}$ is then scaled to uniform by
$CDF_P(p_{combined})$. The PPF is then applied to the scaled $p_{combined}$ resulting in a normally distributed index. The scaling of

230   $p_{combined}$ is numerically slightly unstable and can lead in very rare cases to extremely low SVODI values. Due to the comput-
ers limited precision, these SVODI values always have the exact same value, i.e. -8.14. Therefore, observations where SVODI
is lower than -8 are removed.

Since $p_{combined}$ is always scaled to uniform, the number of available indices at a given time and location does not affect the
distribution of SVODI and a continuous index starting in 1987 to the present is generated. A flag indicates for each SVODI

235   value which sensors and bands contributed to the final value.

3.2   Evaluation methods

SVODI describes the vegetation condition with regard to abnormal vegetation water content. There is no absolute reference to
compare SVODI to and therefore it is evaluated by comparing it to other, well-established vegetation indicators. This is mostly
done by basic correlation analysis, but also by studying temporal shifts and the evolution of extreme values over time. The

240   latter are explained in more detail in the following.

3.2.1   Temporal shift determination

The temporal shifts between SVODI, and VHI and soil moisture anomalies are determined by finding the temporal lag at which
a data set pair correlates the strongest. This is done by grid search, calculating the correlation coefficient for every shift within
a +- 8 week window and selecting for each location the shift with the highest correlation. 8 weeks was chosen because the

245   shifts were found to be almost always less than that, even when searching in a larger window. Then, all results are filtered for

unreliable results: All locations where multiple local maximum shifts were obtained, detected by counting the number of sign changes of the first derivative, or where the maximum correlation coefficient is less than zero, are masked out.

3.2.2 Extreme values over time

250 The plots showing the frequency of extreme values over time are inspired by the plots in Van Der Schrier et al. (2013). For visualization, the data are first standardized to N(0,1) using equation 1. E.g. VHI, TCI and VCI are originally scaled from 0 to 100, and even the N(0,1) distributed indices (e.g. SVODI) are sometimes temporally downsampled, which leads to a reduced variance and therefore requires re-standardization. The percentage of extreme values is then calculated as follows: For a geographical region, for each time step, all pixels with a value greater 1 or 2, respectively, are counted and divided by the total available data points available for that time step.

4 Results and Discussion

255

4.1 Technical analysis

4.1.1 Illustration of the methods by means of an example time series

Figure 3 shows the creation of SVODI at various steps for an exemplary location. The original series have a visible bias between values of the same band (a), which is corrected with the CDF-matching (b). Note that the scaling is done individually for each 260 frequency band and not to a common reference used for all together. E.g., AMSR2, Windsat, and TMI Ku observations are matched to AMSR-E-Ku, etc. Then, an index is created for each sensor and band and the multiple indices are finally merged into SVODI (c). The prior distribution of SVODI is unaffected by the number of observations available at a certain date as the number of available observations varies from 2 to 8 (d), but the SVODI time series shows no breaks between periods with different sensor availability.

265 #### 4.1.2 Extreme values over time

Prior to the SVODI calculation, all datasets are detrended. On a global scale it is therefore expected that the percentage of extreme SVODI values, both positive and negative, is more or less constant over time. Indeed, there seems to be no drastic systematic increase or decrease of the percentage of pixels with |SVODI| greater 1 or 2 (figure 4a). This indicates that even though the number of sensors contributing to SVODI changes over time, this does not lead to massively more or fewer extreme 270 events in a given time period. In contrast, figure 4b shows the percentage of extreme values if SVODI were generated by simply averaging the individual indices per band and sensor, and standardizing the average again. In this case, the periods with few sensors (pre-2002, after 2017) are much more likely to be extreme than the periods with more sensors. This shows that our probabilistic merging method is necessary to compare the frequency of extreme events across different periods.

4.1.3 Impact of the number of input datasets on SVODI

275 If, compared to a simple VODCA standardization, the number of input sensors were to have no effect on the SVODI distribution, then this should be standard normally distributed, irrespective of the number of input sensors. Figure 5 (left) shows the quantiles of SVODI with respect to the quantiles of a standard normal distribution for different numbers of input sensors. Note that this figure is based on random 20% of all data as the whole dataset is too large to be loaded at once. Also, each SVODI value can only be part of one group. Hence, each group distribution is computed from values from different dates.

280

Generally, SVODI is normally distributed regardless of the number of input sensors used for its computation. Only for extremely low values a small difference is observed. Very low values that are also the result of many sensors have a slight positive bias while for very high values this discrepancy does not occur. The cause for this problem is not fully understood, but it is assumed to be related to numerical instability of very low values, as the p-value for days with many observations can become

285 very low. As a simplified numerical example, if a SVODI value is the result of 8 individual uncorrelated indices, and all of them are 0 (indicating average vegetation conditions for all sensors), then the resulting p-value is $CDF(0)^8 = 0.5^8 = 0,004$. This very low value has then to be scaled back to 0.5, and therefore even minor deviations in p can lead to a substantially different p_{scaled}. This example shows that the computation can involve very low values and can therefore become unstable.

Figure 5 (right) shows the quantiles if not our probabilistic merging method was used, but the simple mean of each individual

290 index and standardize the result. It shows that the values of this aggregate index would strongly depend on the number of input observations, as it is much more likely to be extreme if only few input observations are available. This shows that SVODI's dependency on the number of observations is almost removed and a lot lower than if one were to use a simple standardization.

4.1.4 Quality change over time

295 Of interest is whether the quality of SVODI changes over time. There exists no ground-based validation data for VOD, therefore a direct validation with some reference data is not possible. Instead, the spatial correlation to VHI over time is used as an indicator whether SVODI is performing differently during different periods. For each time step, the correlation between the global SVODI and VHI images is calculated. If the signal-to-noise ratio of any of the two data sets would change, so would the correlation between them.

300 The spatial correlation varies quite strongly over time (figure 6a), without having a strong seasonal pattern (figure 6b). This variance is likely due to the varying number of events over time. However, there is a slight positive trend. This is expected, as more and better sensors are progressively becoming available in later years for both SVODI and VHI, resulting in higher quality data for both. In the future, as more advanced sensors are launched into orbit, the two datasets are expected to further converge.

4.2 Data analysis

4.2.1 Comparison of SVODI and VHI

SVODI is compared to VCI, TCI and their composite, the VHI to explore their similarities and differences. By comparing SVODI to all three it is possible to evaluate how it relates to the impact of stress on either vegetation "greenness" (VCI), temperature (TCI) or a combination of both.

Especially in semi-arid climates, SVODI and VHI correlate quite strongly (figure 7a). This is line with previous studies comparing VOD anomalies with LAI, which is also derived from optical data (Moesinger et al., 2020; Jones et al., 2011). The pattern is at least partially due to the more distinct inter- and intra-annual variability of vegetation activity in semi-arid regions. Vegetation in semi-arid regions is highly susceptible to increased or decreased precipitation, and as such they experience stronger anomalies than regions where water is abundant, leading to a higher signal to noise ratio. This then leads to higher correlations between the two indices.

SVODI correlates more strongly with VCI than with TCI (figure 7c and e). This makes sense, as both SVODI and VCI represent *changes* in biogeophysical properties of the canopy as a result of anomalous environmental conditions, whereas TCI mirrors the *effect* of these changes. Since VHI is the average of TCI and VCI, SVODI also correlates more strongly with VCI than with the VHI, especially in cold regions. In semi-arid regions, TCI and SVODI correlate positively because high temperatures lead to unfavourable vegetation conditions and vice versa for low temperatures. Likewise they correlate negatively in cold regions where positive temperature anomalies lead to favourable vegetation conditions and vice versa for low temperature anomalies. (Papagiannopoulou et al., 2017).

Generally, anomalies first occur in TCI followed by VCI and SVODI (figure 7b, d, f), which is expected as there is a causal relationship between prolonged high temperatures in semi-arid regions and a subsequent reduction in vegetation health, and vice versa for low temperatures. VCI generally leading SVODI indicates that changes in greenness occur before changes in vegetation water content. This is to be expected, as reduced photosynthesis is one of the first responses of plants to heat stress, in part due to decay of photosynthetic pigments (Larcher, 2000; Zhao et al., 2020). The plant water content drops more slowly, as plants are able to regulate the rate of transpiration and respiration to balance water loss under transient or mild heat stress (Zhao et al., 2020).

4.2.2 Relation between SVODI and soil moisture at different depths

Correlations between between SVODI and soil moisture anomalies at various depths were calculated to determine the connection between the different depths and the vegetation condition. SVODI and upper level soil moisture anomalies (0 - 7 cm and 7 - 28) correlate strongest with each other in areas where vegetation growth is limited by water availability (figure 8a, c). This is in line with a previous study comparing soil moisture to VOD anomalies (Konings et al., 2021). In areas where vegetation growth is limited by temperature (e.g., see Hashimoto et al. (2019); Papagiannopoulou et al. (2017)), there is generally a negative correlation between SVODI and soil moisture at all levels. This makes sense, as increased precipitation, increased

soil moisture and increased cloud coverage and therefore lower temperatures are all linked to each other in these regions. Additionally, increased soil moisture leads to decreased LST by controlling the partitioning between sensible and latent heat

340 fluxes (Jin Huang and Van Den Dool, 1993). The lower LST then leads to less favourable vegetation conditions in cold regions. This can be also seen if the mean correlation per land cover and depth is considered (figure 9a). In land cover types that are generally found in cold regions, such as needleleaf forests, surface soil moisture anomalies correlate negatively with SVODI and slightly positively with temperature anomalies. The opposite is the case for land cover types generally found in warmer climates (broadleaf forests, shrubs), where more water and lower temperatures lead to more favourable vegetation conditions.

345 Roughly the same pattern is also visible if the analysis is repeated for each season separately (DJF/MAM/JJA/SON[1]), but the pattern shifts with the seasons (results not shown). E.g. in Europe, SVODI correlates negatively with soil moisture in DJF due to the temperature being the limiting factor, but positively in JJA when water is the limiting factor.

Correlation coefficients between SVODI and soil moisture anomalies decrease with increasing depth when no lag optimi-

350 sation is done (figure 9a). However, by optimising the lag the highest correlation coefficients are obtained for 7-28 cm and 28-100 cm soil moisture (figure 9b), even though overall the differences are very small. This agrees with a study showing 7-28 cm to be the most relevant water reservoir for vegetation productivity, particularly in semi-arid regions (Li et al., 2021). The optimised correlation coefficients are highest for land cover types typically found in in arid regions, such as sparse vegetation and shrubs, while they are lowest in needle-leaf forests, which are more often found in regions where temperature is usually

355 more limiting than water.

There is a clear relationship between soil depth and temporal shift (figure 9c), with soil moisture anomalies in layer 3 generally preceding SVODI, and soil moisture anomalies in layer 4 generally following SVODI. This is mostly likely due to bottom level soil moisture levels lagging behind the top ones, which makes sense if moisture is modeled as a "bucket" model where the top layers are filled and depleted first before the lower layers.

360 ### 4.2.3 Sensitivity of SVODI to Australian interannual precipitation variability

The Australian summers of 2010 and 2019 were marked by exceptionally high and low precipitation (figure 10c and e), respectively. 2019 was also exceptionally hot and widespread wildfires occurred (Dunn et al., 2020). As the Australian vegetation is strongly limited by water availability, one would expect that the vegetation moisture content in these years react similarly. Indeed, the SVODI of 2010 and 2019 was exceptionally high/low, respectively (Figure 10a) and the spatial patterns of SVODI

365 and precipitation anomalies are very similar in these periods (Figure 10b and d. This illustrates that SVODI in this water-limited region behaves as expected and is useful to monitor the state of the vegetation.

4.2.4 Effects of drought on vegetation in the Amazon

In the Amazonian rainforest, the extreme values of SVODI, VHI and scPDSI do not agree with each other (figure 11, left column). The effects of droughts in the Amazon forest is a highly discussed topic and very challenging (Samanta et al., 2012).

---

[1]December, January, February, ...

Highly-discussed droughts occurred in 2005, 2010 and 2015 (Panisset et al., 2018; Liu et al., 2018; Lewis et al., 2011; Samanta et al., 2010; Janssen et al., 2021). Some studies argue that the tropical vegetation is light-limited, and as such a decrease in precipitation, which corresponds to a decrease in cloud cover, leads to a greening during droughts (Huete et al., 2006; Saleska et al., 2007). Others argue that the greening is due to artefacts from atmospheric effects and changing sun-sensor geometry (Samanta et al., 2010; Morton et al., 2014). Our results do not give a definitive answer to this discussion, as the patterns are very ambiguous.

4.2.5 Climate oscillation relations to SVODI

The correlation between SVODI, VHI and scPDSI to the Southern Oscillation Index (SOI) (figure 12, left column) and Dipole Mode Index (DMI) (figure 12, right column) are calculated to study how global vegetation is affected by tropical climate oscillations.

SVODI and VHI correlations show a similar pattern. The highest correlation coefficients to SOI are found in eastern Australia, where vegetation is heavily influenced by the El Nino-Southern Oscillation (ENSO) (Liu et al., 2009; Miralles et al., 2014), with high SOI values being linked to increased precipitation. While the scPDSI also agrees with VHI and scPDSI in Australia, it also has a high positive correlation in northern South America and a negative correlation in southern North America and western Asia.

The correlations between SVODI and VHI and DMI are similar and show the greatest magnitude in southern Australia while in most other regions they are close to zero. Correlations between scPDSI and DMI show a more distinguished spatial pattern, including strong positive correlations in northwestern Russia. In this regions, vegetation growth is limited by temperature and not precipitation and for this reason no corresponding patterns can be found in the SVODI or VHI plots.

5 Conclusions

SVODI is a microwave-based vegetation condition index that shows similar patterns as existing optical indices and follows soil moisture in semi-arid regions. It extends the current range of available remote sensing data sets that allow to observe anomalous vegetation states, and increases our understanding of global vegetation dynamics. SVODI patterns are reasonable compared to patterns of VHI, TCI, VCI and soil moisture, but anomalies occur later, which might be an issue for near-real-time applications. With the exception of extreme low values, the proposed index generation method works well at combining different indices. The merging method itself is not limited to VOD and can potentially be applied to combine arbitrary normally-distributed indices. Therefore, this method might find applications in various disciplines. Further efforts will focus on increased numerical stability of the calculations and updating SVODI with more recent observations.

Data availability. [Will be added once paper is through review]

400   *Author contributions.* WD and LM designed the study. LM performed the analyses and wrote the paper together with WD. All authors contributed to discussions about the methods and results and provided feedback on the paper.

Competing interests. The authors declare that they have no conflict of interest.

References

Aldred, F., Gobron, N., Miller, J. B., Willett, K. M., and Dunn, R.: Global climate, https://doi.org/10.1175/BAMS-D-21-0098.1, 2021.

405 Allan, R.: Können. G. P., Jones, P. D., Katofen, M. H. and Allan, R. J., 1998: Pre-1866 extensions of the Southern Oscillation Index using early Indonesian and Tahitian meteorological readings. Journal of Climate, 11, (9). 2325-2339., 1998.

Allan, R. J., Nicholls, N., Jones, P. D., and Butterworth, I. J.: A Further Extension of the Tahiti–Darwin SOI, Early ENSO Events and Darwin Pressure, Journal of Climate, 4, 743–749, http://www.jstor.org/stable/26196423, 1991.

Crocetti, L., Forkel, M., Fischer, M., Jurečka, F., Grlj, A., Salentinig, A., Trnka, M., Anderson, M., Ng, W.-T., Kokalj, Ž., Bucur, A., and
410 Dorigo, W.: Earth Observation for agricultural drought monitoring in the Pannonian Basin (southeastern Europe): current state and future directions, Regional Environmental Change, 20, 123, https://doi.org/10.3929/ETHZ-B-000459516, 2020.

Dorigo, W., Wagner, W., Albergel, C., Albrecht, F., Balsamo, G., Brocca, L., Chung, D., Ertl, M., Forkel, M., Gruber, A., Haas, E., Hamer, P. D., Hirschi, M., Ikonen, J., de Jeu, R., Kidd, R., Lahoz, W., Liu, Y. Y., Miralles, D., Mistelbauer, T., Nicolai-Shaw, N., Parinussa, R., Pratola, C., Reimer, C., van der Schalie, R., Seneviratne, S. I., Smolander, T., and Lecomte, P.: ESA CCI Soil Mois-
415 ture for improved Earth system understanding: State-of-the art and future directions, Remote Sensing of Environment, 203, 185–215, https://doi.org/10.1016/j.rse.2017.07.001, http://linkinghub.elsevier.com/retrieve/pii/S0034425717303061, 2017.

Dorigo, W. A., Zurita-Milla, R., de Wit, A. J., Brazile, J., Singh, R., and Schaepman, M. E.: A review on reflective remote sensing and data assimilation techniques for enhanced agroecosystem modeling, International Journal of Applied Earth Observation and Geoinformation, 9, 165–193, https://doi.org/10.1016/j.jag.2006.05.003, 2007.

420 Dunn, R. J., Stanitski, D. M., Gobron, N., and Willett, K. M.: Global climate, https://doi.org/10.1175/BAMS-D-20-0104.1, 2020.

Frappart, F., Wigneron, J.-P., Li, X., Liu, X., Al-Yaari, A., Fan, L., Wang, M., Moisy, C., Le Masson, E., Aoulad Lafkih, Z., Vallé, C., Ygorra, B., and Baghdadi, N.: Global Monitoring of the Vegetation Dynamics from the Vegetation Optical Depth (VOD): A Review, Remote Sensing, 12, 2915, https://doi.org/10.3390/rs12182915, https://www.mdpi.com/2072-4292/12/18/2915, 2020.

Gaiser, P. W., St. Germain, K. M., Twarog, E. M., Poe, G. A., Purdy, W., Richardson, D., Grossman, W., Jones, W. L., Spencer,
425 D., Golba, G., Cleveland, J., Choy, L., Bevilacqua, R. M., and Chang, P. S.: The windSat spaceborne polarimetric microwave radiometer: Sensor description and early orbit performance, IEEE Transactions on Geoscience and Remote Sensing, 42, 2347–2361, https://doi.org/10.1109/TGRS.2004.836867, 2004.

Guo, Y., Huang, S., Huang, Q., Wang, H., Fang, W., Yang, Y., and Wang, L.: Assessing socioeconomic drought based on an improved Multivariate Standardized Reliability and Resilience Index, Journal of Hydrology, 568, 904–918, https://doi.org/10.1016/j.jhydrol.2018.11.055,
430 https://doi.org/10.1016/j.jhydrol.2018.11.055, 2019.

Hao, Z. and AghaKouchak, A.: Multivariate Standardized Drought Index: A parametric multi-index model, Advances in Water Resources, 57, 12–18, https://doi.org/10.1016/j.advwatres.2013.03.009, http://dx.doi.org/10.1016/j.advwatres.2013.03.009, 2013.

Hashimoto, H., Nemani, R., Bala, G., Cao, L., Michaelis, A., Ganguly, S., Wang, W., Milesi, C., Eastman, R., Lee, T., and Myneni, R.: Constraints to Vegetation Growth Reduced by Region-Specific Changes in Seasonal Climate, Climate, 7, 27,
435 https://doi.org/10.3390/cli7020027, https://www.mdpi.com/2225-1154/7/2/27, 2019.

Hersbach, H., Bell, B., Berrisford, P., Hirahara, S., Horányi, A., Muñoz-Sabater, J., Nicolas, J., Peubey, C., Radu, R., Schepers, D., Simmons, A., Soci, C., Abdalla, S., Abellan, X., Balsamo, G., Bechtold, P., Biavati, G., Bidlot, J., Bonavita, M., Chiara, G., Dahlgren, P., Dee, D., Diamantakis, M., Dragani, R., Flemming, J., Forbes, R., Fuentes, M., Geer, A., Haimberger, L., Healy, S., Hogan, R. J., Hólm, E., Janisková, M., Keeley, S., Laloyaux, P., Lopez, P., Lupu, C., Radnoti, G., Rosnay, P., Rozum, I., Vamborg, F., Villaume, S., and Thépaut,

440   J.: The ERA5 global reanalysis, Quarterly Journal of the Royal Meteorological Society, 146, 1999–2049, https://doi.org/10.1002/qj.3803, https://onlinelibrary.wiley.com/doi/10.1002/qj.3803, 2020.

Holmes, T. R. H., De Jeu, R. A. M., Owe, M., and Dolman, A. J.: Land surface temperature from Ka band (37 GHz) passive microwave observations, Journal of Geophysical Research, 114, D04 113, https://doi.org/10.1029/2008JD010257, http://doi.wiley.com/10.1029/2008JD010257, 2009.

445   Huang, S., Tang, L., Hupy, J. P., Wang, Y., and Shao, G.: A commentary review on the use of normalized difference vegetation index (NDVI) in the era of popular remote sensing, https://doi.org/10.1007/s11676-020-01155-1, 2021.

Huete, A. R., Didan, K., Shimabukuro, Y. E., Ratana, P., Saleska, S. R., Hutyra, L. R., Yang, W., Nemani, R. R., and Myneni, R.: Amazon rainforests green-up with sunlight in dry season, Geophysical Research Letters, 33, L06 405, https://doi.org/10.1029/2005GL025583, http://doi.wiley.com/10.1029/2005GL025583, 2006.

450   Iturbide, M., Gutiérrez, J. M., Alves, L. M., Bedia, J., Cerezo-Mota, R., Cimadevilla, E., Cofiño, A. S., Luca, A. D., Faria, S. H., Gorodetskaya, I. V., Hauser, M., Herrera, S., Hennessy, K., Hewitt, H. T., Jones, R. G., Krakovska, S., Manzanas, R., Martínez-Castro, D., Narisma, G. T., Nurhati, I. S., Pinto, I., Seneviratne, S. I., van den Hurk, B., and Vera, C. S.: An update of IPCC climate reference regions for subcontinental analysis of climate model data: definition and aggregated datasets, Earth System Science Data, 12, 2959–2970, https://doi.org/10.5194/essd-12-2959-2020, 2020.

455   Jackson, T. and Schmugge, T.: Vegetation effects on the microwave emission of soils, Remote Sensing of Environment, 36, 203–212, https://doi.org/10.1016/0034-4257(91)90057-D, https://www.sciencedirect.com/science/article/pii/003442579190057D, 1991.

Janssen, T., van der Velde, Y., Hofhansl, F., Luyssaert, S., Naudts, K., Driessen, B., Fleischer, K., and Dolman, H.: Drought effects on leaf fall, leaf flushing and stem growth in the Amazon forest: reconciling remote sensing data and field observations, Biogeosciences, 18, 4445–4472, https://doi.org/10.5194/bg-18-4445-2021, https://bg.copernicus.org/articles/18/4445/2021/, 2021.

460   Jin Huang and Van Den Dool, H. M.: Monthly precipitation-temperature relations and temperature prediction over the United States, Journal of Climate, 6, 1111–1132, https://doi.org/10.1175/1520-0442(1993)006<1111:mptrat>2.0.co;2, 1993.

Jones, M. O., Jones, L. A., Kimball, J. S., and McDonald, K. C.: Satellite passive microwave remote sensing for monitoring global land surface phenology, Remote Sensing of Environment, 115, 1102–1114, https://doi.org/10.1016/J.RSE.2010.12.015, https://www.sciencedirect.com/science/article/pii/S0034425710003615, 2011.

465   Katz, R. W. and Glantz, M. H.: Anatomy of a rainfall index., Monthly Weather Review, 114, 764–771, https://doi.org/10.1175/1520-0493(1986)114<0764:AOARI>2.0.CO;2, 1986.

Kawanishi, T., Sezai, T., Ito, Y., Imaoka, K., Takeshima, T., Ishido, Y., Shibata, A., Miura, M., Inahata, H., and Spencer, R.: The advanced microwave scanning radiometer for the earth observing system (AMSR-E), NASDA's contribution to the EOS for global energy and water cycle studies, IEEE Transactions on Geoscience and Remote Sensing, 41, 184–194, https://doi.org/10.1109/TGRS.2002.808331, 470   http://ieeexplore.ieee.org/document/1196037/, 2003.

Knowles, K., Savoie, M., Armstrong, R., and Brodzik, M. J.: AMSR-E/Aqua Daily EASE-Grid Brightness Temperatures, https://doi.org/https://doi.org/10.5067/XIMNXRTQVMOX, 2006.

Kogan, F. N.: Remote sensing of weather impacts on vegetation in non-homogeneous areas, International Journal of Remote Sensing, 11, 1405–1419, https://doi.org/10.1080/01431169008955102, 1990.

475   Kogan, F. N.: Global Drought Watch from Space, Bulletin of the American Meteorological Society, 78, 621–636, https://doi.org/10.1175/1520-0477(1997)078<0621:GDWFS>2.0.CO;2, 1997.

Kogan, F. N.: Operational space technology for global vegetation assessment, Bulletin of the American Meteorological Society, 82, 1949–1964, https://doi.org/10.1175/1520-0477(2001)082<1949:OSTFGV>2.3.CO;2, 2001.

Konings, A. G., Holtzman, N. M., Rao, K., Xu, L., and Saatchi, S. S.: Interannual Variations of Vegetation Optical Depth are Due to Both
480   Water Stress and Biomass Changes, Geophysical Research Letters, 48, e2021GL095 267, https://doi.org/10.1029/2021gl095267, 2021.

Kummerow, C., Barnes, W., Kozu, T., Shiue, J., Simpson, J., Kummerow, C., Barnes, W., Kozu, T., Shiue, J., and Simpson, J.: The Tropical Rainfall Measuring Mission (TRMM) Sensor Package, Journal of Atmospheric and Oceanic Technology, 15, 809–817, https://doi.org/10.1175/1520-0426(1998)015<0809:TTRMMT>2.0.CO;2, http://journals.ametsoc.org/doi/abs/10.1175/1520-0426%281998%29015%3C0809%3ATTRMMT%3E2.0.CO%3B2, 1998.

485 Larcher, W.: Temperature stress and survival ability of mediterranean sclerophyllous plants, Plant Biosystems, 134, 279–295, https://doi.org/10.1080/11263500012331350455, 2000.

Lewis, S. L., Brando, P. M., Phillips, O. L., Van Der Heijden, G. M., and Nepstad, D.: The 2010 Amazon drought, https://doi.org/10.1126/science.1200807, 2011.

Li, W., Migliavacca, M., Forkel, M., Walther, S., Reichstein, M., and Orth, R.: Revisiting Global Vegetation Controls Using Multi-Layer Soil
490   Moisture, Geophysical Research Letters, 48, e2021GL092 856, https://doi.org/10.1029/2021GL092856, 2021.

Liu, Y. Y., van Dijk, A. I. J. M., de Jeu, R. A. M., and Holmes, T. R. H.: An analysis of spatiotemporal variations of soil and vegetation moisture from a 29-year satellite-derived data set over mainland Australia, Water Resources Research, 45, https://doi.org/10.1029/2008WR007187, http://doi.wiley.com/10.1029/2008WR007187, 2009.

Liu, Y. Y., Van Dijk, A. I., De Jeu, R. A., Canadell, J. G., McCabe, M. F., Evans, J. P., and Wang, G.: Recent reversal in loss of global
495   terrestrial biomass, Nature Climate Change, 5, 470–474, https://doi.org/10.1038/nclimate2581, 2015.

Liu, Y. Y., van Dijk, A. I., Miralles, D. G., McCabe, M. F., Evans, J. P., de Jeu, R. A., Gentine, P., Huete, A., Parinussa, R. M., Wang, L., Guan, K., Berry, J., and Restrepo-Coupe, N.: Enhanced canopy growth precedes senescence in 2005 and 2010 Amazonian droughts, Remote Sensing of Environment, 211, 26–37, https://doi.org/10.1016/J.RSE.2018.03.035, https://www.sciencedirect.com/science/article/pii/S0034425718301366, 2018.

500 Martens, B., Miralles, D. G., Lievens, H., Van Der Schalie, R., De Jeu, R. A., Fernández-Prieto, D., Beck, H. E., Dorigo, W. A., and Verhoest, N. E.: GLEAM v3: Satellite-based land evaporation and root-zone soil moisture, Geoscientific Model Development, 10, 1903–1925, https://doi.org/10.5194/gmd-10-1903-2017, 2017.

Martens, B., Waegeman, W., Dorigo, W. A., Verhoest, N. E., and Miralles, D. G.: Terrestrial evaporation response to modes of climate variability, npj Climate and Atmospheric Science, 1, 1–7, https://doi.org/10.1038/s41612-018-0053-5, 2018.

505 Meesters, A., DeJeu, R., and Owe, M.: Analytical Derivation of the Vegetation Optical Depth From the Microwave Polarization Difference Index, IEEE Geoscience and Remote Sensing Letters, 2, 121–123, https://doi.org/10.1109/LGRS.2005.843983, http://ieeexplore.ieee.org/document/1420287/, 2005.

Meier, W., JesefinoC, C., and Thorsten, M.: NRT AMSR2 Unified L3 Daily 25 km Brightness Temperature and Sea Ice Concentration Polar Grids V1, https://doi.org/undefined, http://undefined, 2018.

510 Miralles, D. G., Van Den Berg, M. J., Gash, J. H., Parinussa, R. M., De Jeu, R. A., Beck, H. E., Holmes, T. R., Jiménez, C., Verhoest, N. E., Dorigo, W. A., Teuling, A. J., and Johannes Dolman, A.: El Niño-La Niña cycle and recent trends in continental evaporation, Nature Climate Change, 4, 122–126, https://doi.org/10.1038/nclimate2068, 2014.

Mo, T., Choudhury, B. J., Schmugge, T. J., Wang, J. R., and Jackson, T. J.: A model for microwave emission from vegetation-covered fields, Journal of Geophysical Research, 87, 11 229, https://doi.org/10.1029/JC087iC13p11229, http://doi.wiley.com/10.1029/JC087iC13p11229, 1982.

Moesinger, L., Dorigo, W., De Jeu, R., Van Der Schalie, R., Scanlon, T., Teubner, I., and Forkel, M.: The global long-term microwave Vegetation Optical Depth Climate Archive (VODCA), Earth System Science Data, 12, 177–196, https://doi.org/10.5194/essd-12-177-2020, 2020.

Morton, D. C., Nagol, J., Carabajal, C. C., Rosette, J., Palace, M., Cook, B. D., Vermote, E. F., Harding, D. J., and North, P. R. J.: Amazon forests maintain consistent canopy structure and greenness during the dry season, Nature, 506, 221–224, https://doi.org/10.1038/nature13006, http://www.nature.com/articles/nature13006, 2014.

Muñoz-Sabater, J., Dutra, E., Agustí-Panareda, A., Albergel, C., Arduini, G., Balsamo, G., Boussetta, S., Choulga, M., Harrigan, S., Hersbach, H., Martens, B., Miralles, D. G., Piles, M., Rodríguez-Fernández, N. J., Zsoter, E., Buontempo, C., and Thépaut, J. N.: ERA5-Land: A state-of-the-art global reanalysis dataset for land applications, Earth System Science Data, 13, 4349–4383, https://doi.org/10.5194/essd-13-4349-2021, 2021.

Owe, M., de Jeu, R., and Holmes, T.: Multisensor historical climatology of satellite-derived global land surface moisture, Journal of Geophysical Research, 113, F01 002, https://doi.org/10.1029/2007JF000769, http://doi.wiley.com/10.1029/2007JF000769, 2008.

Palmer, W. C.: Meteorological drought, vol. 30, US Department of Commerce, Weather Bureau, 1965.

Panisset, J. S., Libonati, R., Gouveia, C. M. P., Machado-Silva, F., França, D. A., França, J. R. A., and Peres, L. F.: Contrasting patterns of the extreme drought episodes of 2005, 2010 and 2015 in the Amazon Basin, International Journal of Climatology, 38, 1096–1104, https://doi.org/10.1002/joc.5224, http://doi.wiley.com/10.1002/joc.5224, 2018.

Papagiannopoulou, C., Miralles, D. G., Dorigo, W. A., Verhoest, N. E., Depoorter, M., and Waegeman, W.: Vegetation anomalies caused by antecedent precipitation in most of the world, Environmental Research Letters, 12, 074 016, https://doi.org/10.1088/1748-9326/aa7145, 2017.

Pause, M., Schweitzer, C., Rosenthal, M., Keuck, V., Bumberger, J., Dietrich, P., Heurich, M., Jung, A., and Lausch, A.: In Situ/Remote Sensing Integration to Assess Forest Health—A Review, Remote Sensing, 8, 471, https://doi.org/10.3390/rs8060471, http://www.mdpi.com/2072-4292/8/6/471, 2016.

Petersen, L.: Real-Time Prediction of Crop Yields From MODIS Relative Vegetation Health: A Continent-Wide Analysis of Africa, Remote Sensing, 10, 1726, https://doi.org/10.3390/rs10111726, http://www.mdpi.com/2072-4292/10/11/1726, 2018.

Rodríguez-Pérez, J. R., Ordóñez, C., González-Fernández, A. B., Sanz-Ablanedo, E., Valenciano, J. B., and Marcelo, V.: Leaf water content estimation by functional linear regression of field spectroscopy data, Biosystems Engineering, 165, 36–46, https://doi.org/10.1016/J.BIOSYSTEMSENG.2017.08.017, https://www.sciencedirect.com/science/article/pii/S1537511017308334, 2018.

Saji, N. H. and Yamagata, T.: Possible impacts of Indian Ocean Dipole mode events on global climate, Climate Research, 25, 151–169, https://doi.org/10.3354/CR025151, 2003.

Saji, N. H., Goswami, B. N., Vinayachandran, P. N., and Yamagata, T.: A dipole mode in the tropical Indian Ocean, Nature 1999 401:6751, 401, 360–363, https://doi.org/10.1038/43854, https://www.nature.com/articles/43854, 1999.

Saleska, S. R., Didan, K., Huete, A. R., and da Rocha, H. R.: Amazon forests green-up during 2005 drought., Science (New York, N.Y.), 318, 612, https://doi.org/10.1126/science.1146663, http://www.ncbi.nlm.nih.gov/pubmed/17885095, 2007.

550 Samanta, A., Ganguly, S., Hashimoto, H., Devadiga, S., Vermote, E., Knyazikhin, Y., Nemani, R. R., and Myneni, R. B.: Amazon forests
did not green-up during the 2005 drought, Geophysical Research Letters, 37, n/a–n/a, https://doi.org/10.1029/2009GL042154, http://doi.
wiley.com/10.1029/2009GL042154, 2010.

Samanta, A., Ganguly, S., Vermote, E., Nemani, R. R., and Myneni, R. B.: Why Is Remote Sensing of Amazon Forest Greenness So
Challenging?, Earth Interactions, 16, 1–14, https://doi.org/10.1175/2012EI440.1, http://journals.ametsoc.org/doi/abs/10.1175/2012EI440.
555 1https://journals.ametsoc.org/doi/10.1175/2012EI440.1, 2012.

Szpakowski, D. M. and Jensen, J. L.: A review of the applications of remote sensing in fire ecology, https://doi.org/10.3390/rs11222638,
2019.

Thomas B. McKee, N. J. D. and Kleist, J.: Analysis of Standardized Precipitation Index (SPI) data for drought assessment,
Water (Switzerland), 26, 1–72, https://doi.org/10.1088/1755-1315/5, http://dx.doi.org/10.1016/j.wace.2014.12.001%0Ahttp:
560 //dx.doi.org/10.1016/j.wace.2015.05.002%0Awww.uniquindio.edu.co%0Ahttp://www.fao.org/3/a-i5695e.pdf%0Ahttp://dx.doi.org/
10.1016/j.desal.2015.03.029%0Ahttp://www.sciencedirect.com/science/article/pii/S136, 1993.

Tucker, C. J., Pinzon, J. E., Brown, M. E., Slayback, D. A., Pak, E. W., Mahoney, R., Vermote, E. F., and El Saleous, N.: An extended AVHRR
8-km NDVI dataset compatible with MODIS and SPOT vegetation NDVI data, International Journal of Remote Sensing, 26, 4485–4498,
https://doi.org/10.1080/01431160500168686, https://www.tandfonline.com/doi/full/10.1080/01431160500168686, 2005.

565 van der Schalie, R., de Jeu, R., Kerr, Y., Wigneron, J., Rodríguez-Fernández, N., Al-Yaari, A., Parinussa, R., Mecklenburg, S., and Drusch,
M.: The merging of radiative transfer based surface soil moisture data from SMOS and AMSR-E, Remote Sensing of Environment, 189,
180–193, https://doi.org/10.1016/J.RSE.2016.11.026, https://www.sciencedirect.com/science/article/pii/S0034425716304734, 2017.

Van Der Schrier, G., Barichivich, J., Briffa, K. R., and Jones, P. D.: A scPDSI-based global data set of dry and wet spells for 1901-2009,
Journal of Geophysical Research Atmospheres, 118, 4025–4048, https://doi.org/10.1002/jgrd.50355, 2013.

570 van Marle, M. J. E., van der Werf, G. R., de Jeu, R. A. M., and Liu, Y. Y.: Annual South American forest loss estimates based on passive
microwave remote sensing (1990–2010), Biogeosciences Discussions, 12, 11 499–11 535, https://doi.org/10.5194/bgd-12-11499-2015,
http://www.biogeosciences-discuss.net/12/11499/2015/, 2015.

Vogelmann, J. E., Xian, G., Homer, C., and Tolk, B.: Monitoring gradual ecosystem change using Landsat time series analyses: Case studies
in selected forest and rangeland ecosystems, Remote Sensing of Environment, 122, 92–105, https://doi.org/10.1016/j.rse.2011.06.027,
575 2012.

Vreugdenhil, M., Navacchi, C., Bauer-Marschallinger, B., Hahn, S., Steele-Dunne, S., Pfeil, I., Dorigo, W., and Wagner, W.: Sentinel-1
Cross Ratio and Vegetation Optical Depth: A Comparison over Europe, Remote Sensing, 12, 3404, https://doi.org/10.3390/rs12203404,
https://www.mdpi.com/2072-4292/12/20/3404, 2020.

Wells, N., Goddard, S., and Hayes, M. J.: A self-calibrating Palmer Drought Severity Index, Journal of Climate, 17, 2335–2351,
580 https://doi.org/10.1175/1520-0442(2004)017<2335:ASPDSI>2.0.CO;2, 2004.

Wentz, F. J.: A well-calibrated ocean algorithm for special sensor microwave / imager, Journal of Geophysical Research: Oceans, 102,
8703–8718, https://doi.org/10.1029/96JC01751, http://doi.wiley.com/10.1029/96JC01751, 1997.

Zhao, J., Lu, Z., Wang, L., and Jin, B.: Plant Responses to Heat Stress: Physiology, Transcription, Noncoding RNAs, and Epigenetics,
International Journal of Molecular Sciences, 22, 117, https://doi.org/10.3390/ijms22010117, https://www.mdpi.com/1422-0067/22/1/117,
585 2020.

Table 1. Overview of VOD data sets used in this study with their temporal coverage, local ascending equatorial crossing times (AETC), whether the (A)scending or (D)escending overpass is used, and used frequencies [GHz] for each product. The C- and X-band retrievals are based on van der Schalie et al. (2017), the Ku-band retrievals on Owe et al. (2008).

Sensor	Time period used	AECT	Overpass	C-Band	X-Band	Ku-Band
AMSR-E	Jun 2002 - Oct 2011	13:30	D	6.93	10.65	18.7
AMSR2	Jul 2012 - Jan 2020	13:30	D	6.93 & 7.3	10.65	18.7
SSM/I F08	Jul 1987 - Dec 1991	18:15	A			19.35
SSM/I F11	Dec 1991 - May 1995	17:00 - 18:15	D			19.35
SSM/I F13	May 1995 - Apr 2009	17:45 - 18:40	D			19.35
TMI	Dec 1997 - Apr 2015	Asynchronous	Mix		10.65	19.35
WindSat	Feb 2003 - Jul 2012	18:00	D	6.8	10.7	18.7
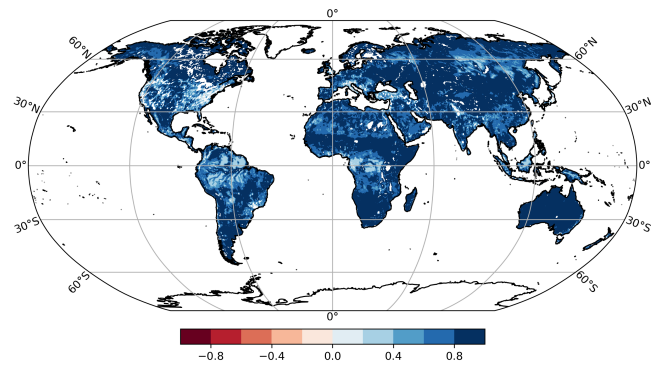
(a) C vs. X
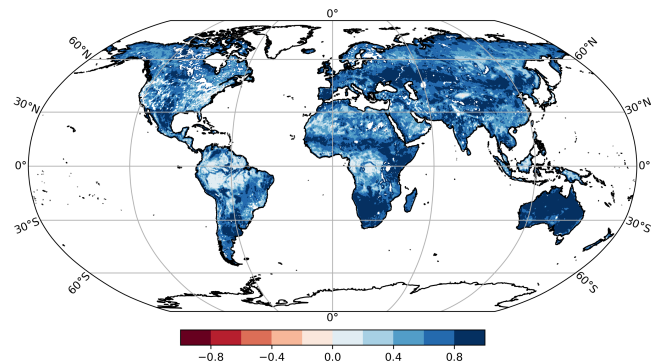
(b) C vs. Ku
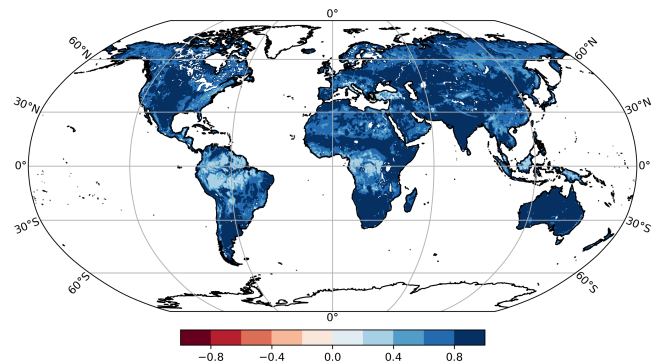
(c) X vs. Ku

Figure 1. Exemplary correlation coefficients between C-, X- and Ku-VOD anomalies of AMSR-E, derived with the LPRM Model (section 2.1.1). Similar results are obtained for other sensors (not shown).
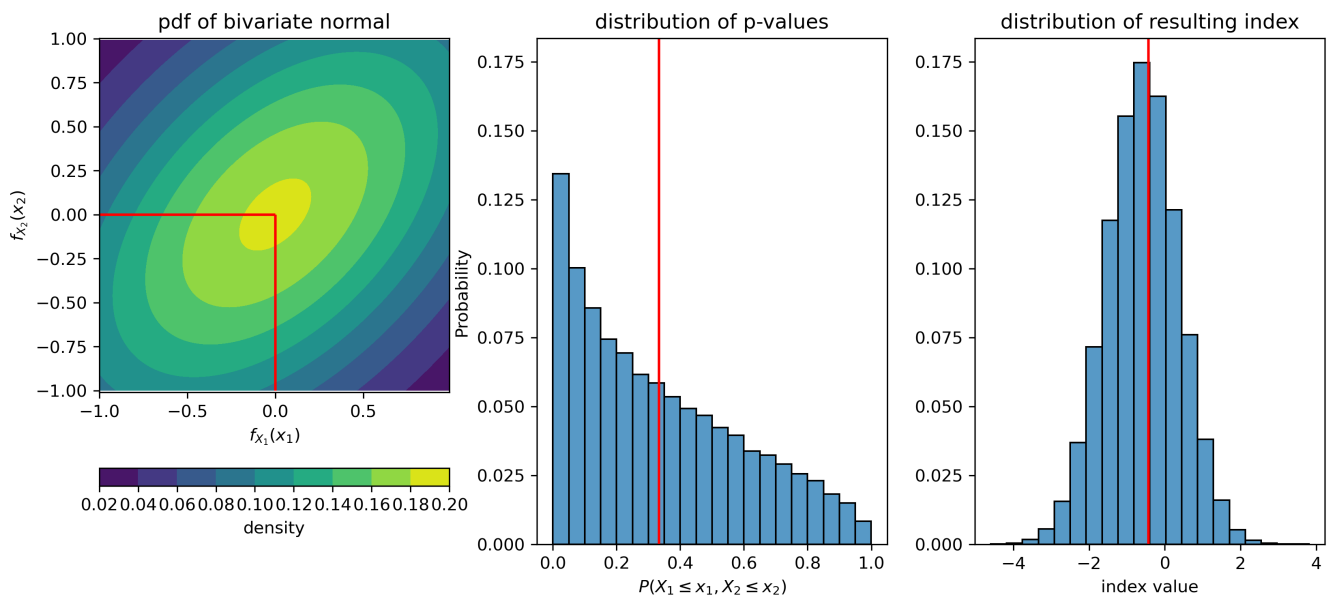
Figure 2. Bi-variate example of a probabilistic multivariate index as in Hao and AghaKouchak (2013); Guo et al. (2019) without scaling of p where X_1, X_2 $N(0,1)$ and the covariance between them is 0.5. PDF (left), distribution of the CDF of samples from it (middle) and the resulting distribution of the index (right). The red lines mark an example case where $x_1 = x_2 = 0$ at different processing steps.
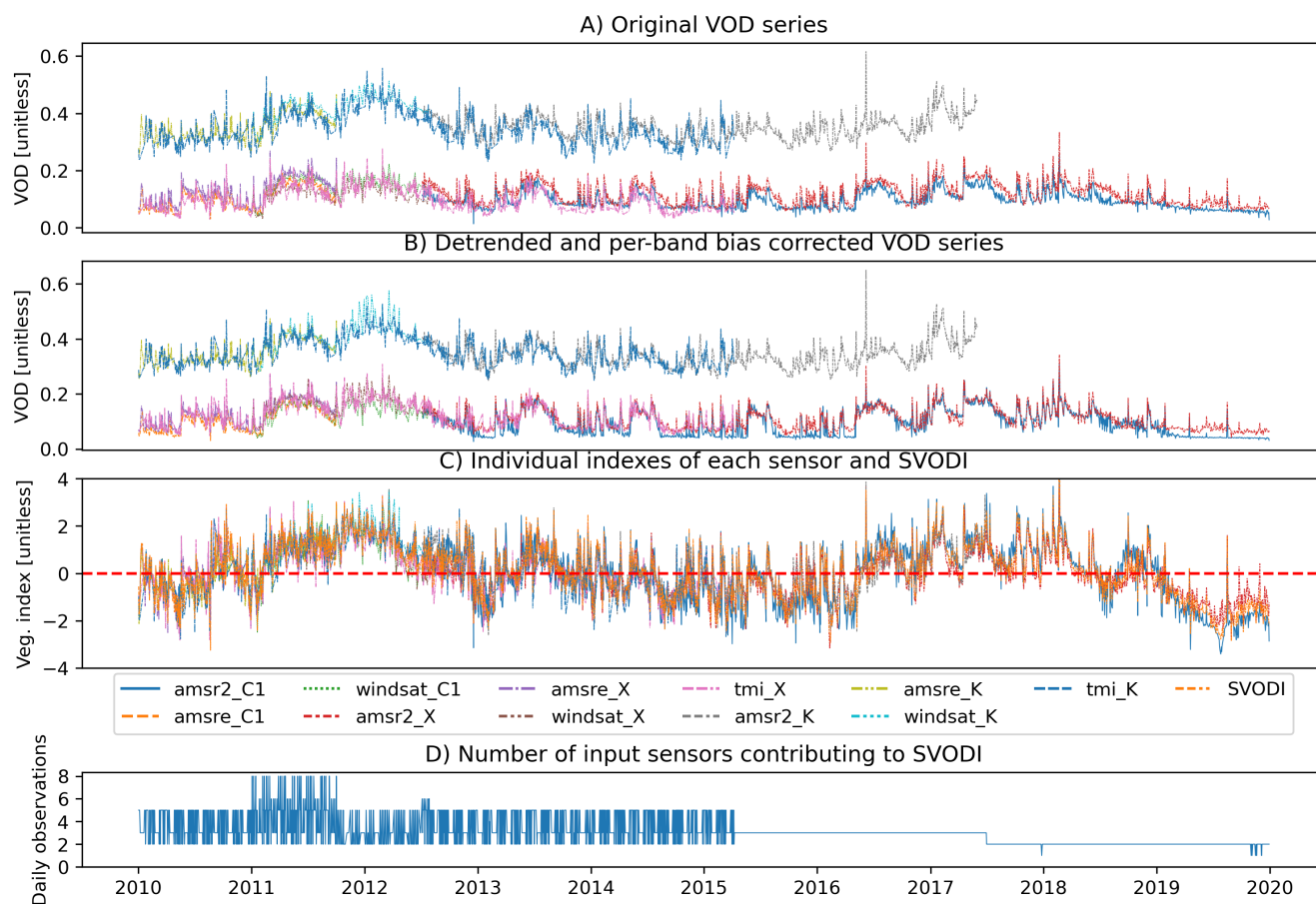
Figure 3. Temporal subset of an example time series at different processing stages in Western Australia, 24.9S, 125.625E, located in the Gibson Desert Nature Reserve. The vegetation is shrubland with sparse trees. a) Original VOD time series. b) The same VOD-series after bias correction. Note that only the bias within each band is corrected and not to a common reference for all bands. c) The indexes created from each sensor and band as well as SVODI. d) The number of observations contributing to a SVODI value for each day.
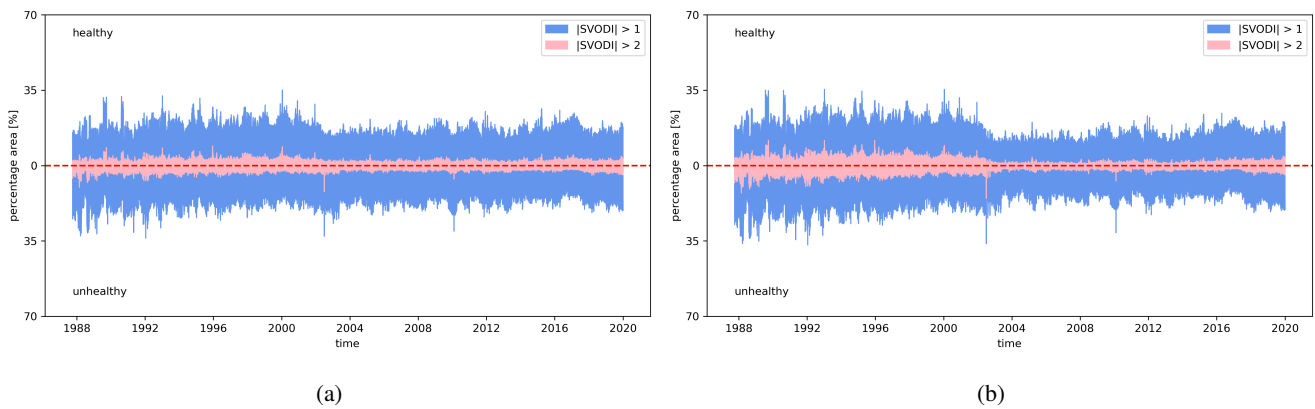
Figure 4. Fraction of pixels being extreme of SVODI (a) and non-probabilistic merge of indices (b) over time.
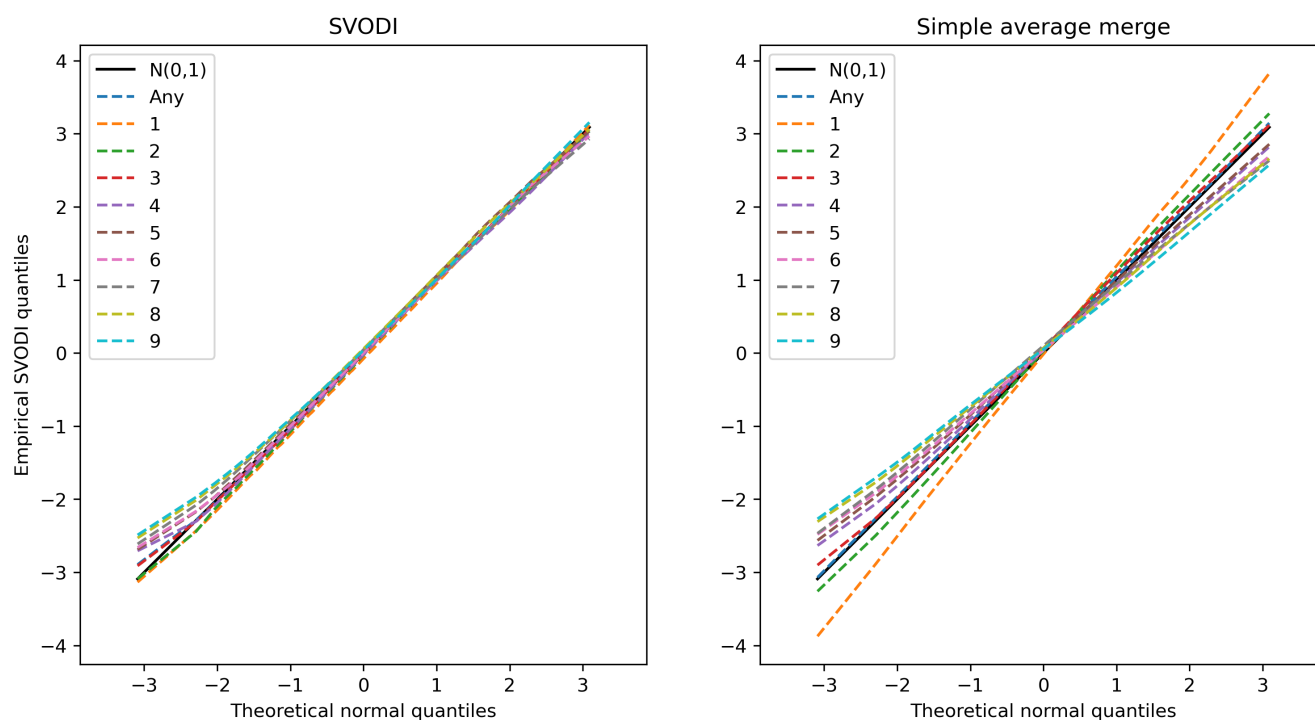
Figure 5. QQ-plots for different number of input observations. E.g. "3" shows the quantiles of all SVODI values where three input indexes contributed. "Any" shows the quantiles for any number of observations. N(0,1), the diagonal, shows theoretical normal distribution for comparison. Left shows the quantile-quantile plot of SVODI, right shows for comparison the quantiles of an index generated by simple averaging.

(a)   (b)
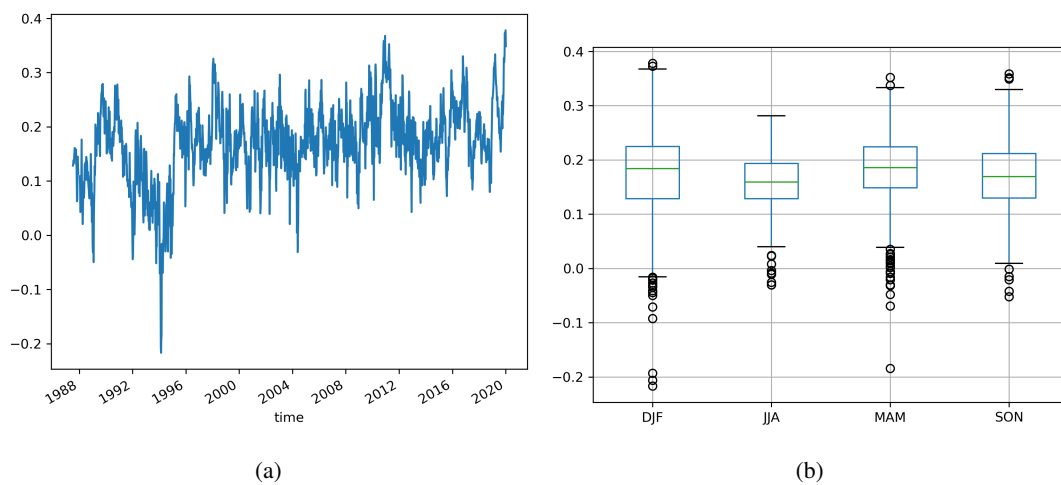
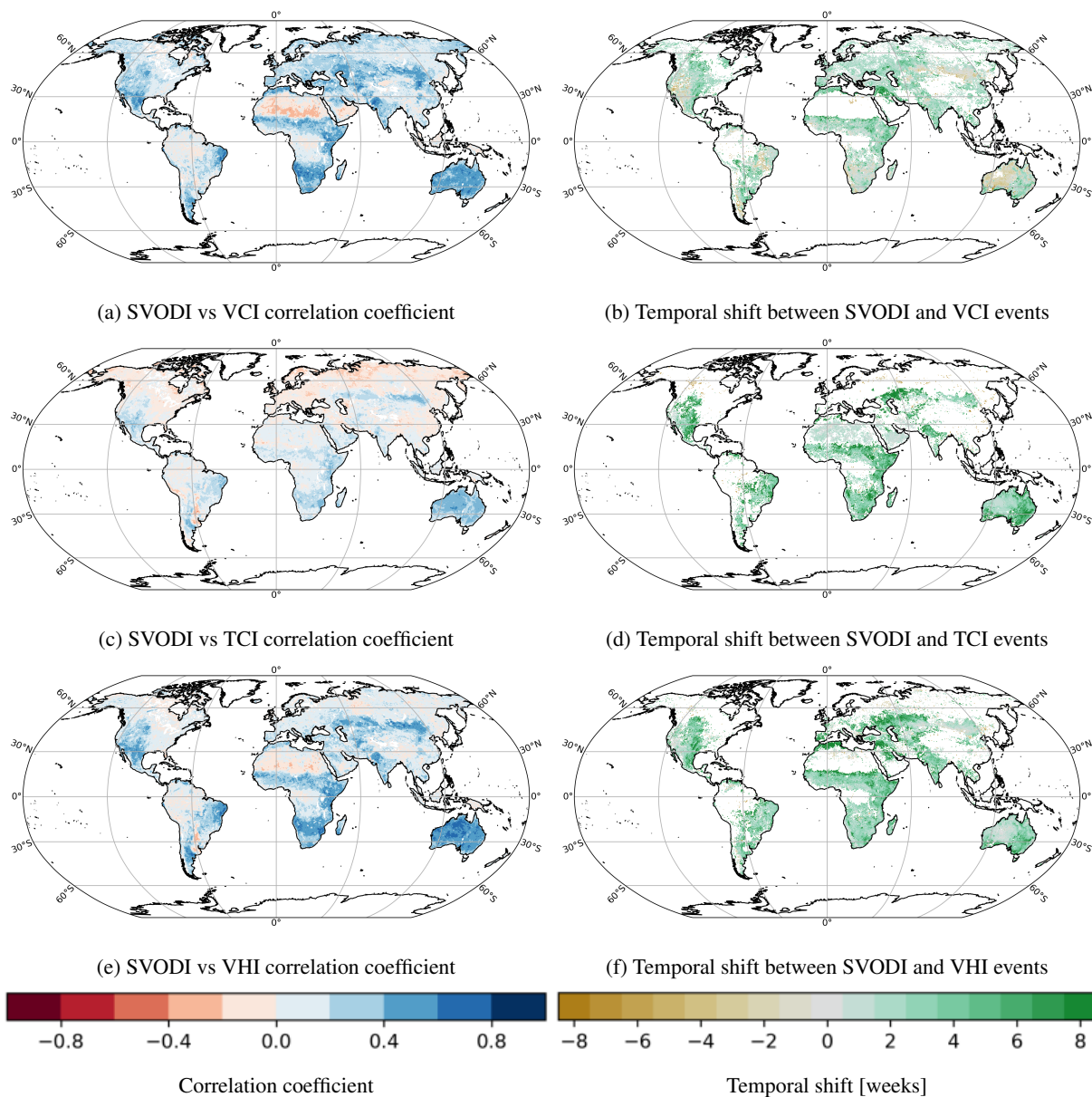**Figure 6.** Spatial correlation coefficient of SVODI vs VHI over time (a) and per season (b). Based on weekly data.

(a) SVODI vs VCI correlation coefficient

(b) Temporal shift between SVODI and VCI events

(c) SVODI vs TCI correlation coefficient

(d) Temporal shift between SVODI and TCI events

(e) SVODI vs VHI correlation coefficient

(f) Temporal shift between SVODI and VHI events

Correlation coefficient

Temporal shift [weeks]

Figure 7. Correlation coefficient without temporal shift between SVODI and VCI (a), TCI (c) and VHI (e), respectively and the temporal shift at which a maximum correlation is obtained (b, d, f). All results are based on weekly means, positive (green) values in the shift plots indicate that anomalies are visible in VCI/TCI/VHI before SVODI.
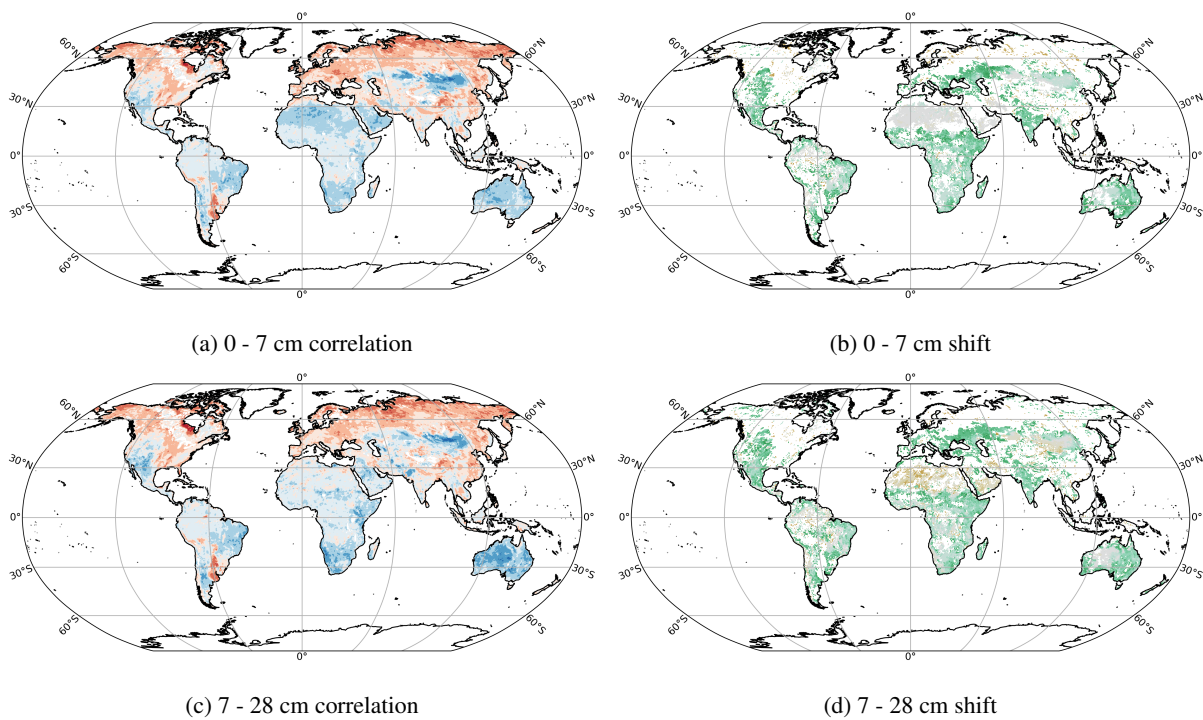
27

(a) 0 - 7 cm correlation

(b) 0 - 7 cm shift

(c) 7 - 28 cm correlation

(d) 7 - 28 cm shift

Figure 8. Correlation (left column) and temporal shift (right column) between SVODI and soil moisture anomalies from ERA5, based on weekly data. Positive (green) values in the shift plots indicate that anomalies are earlier visible in soil moisture than in SVODI. (first part)
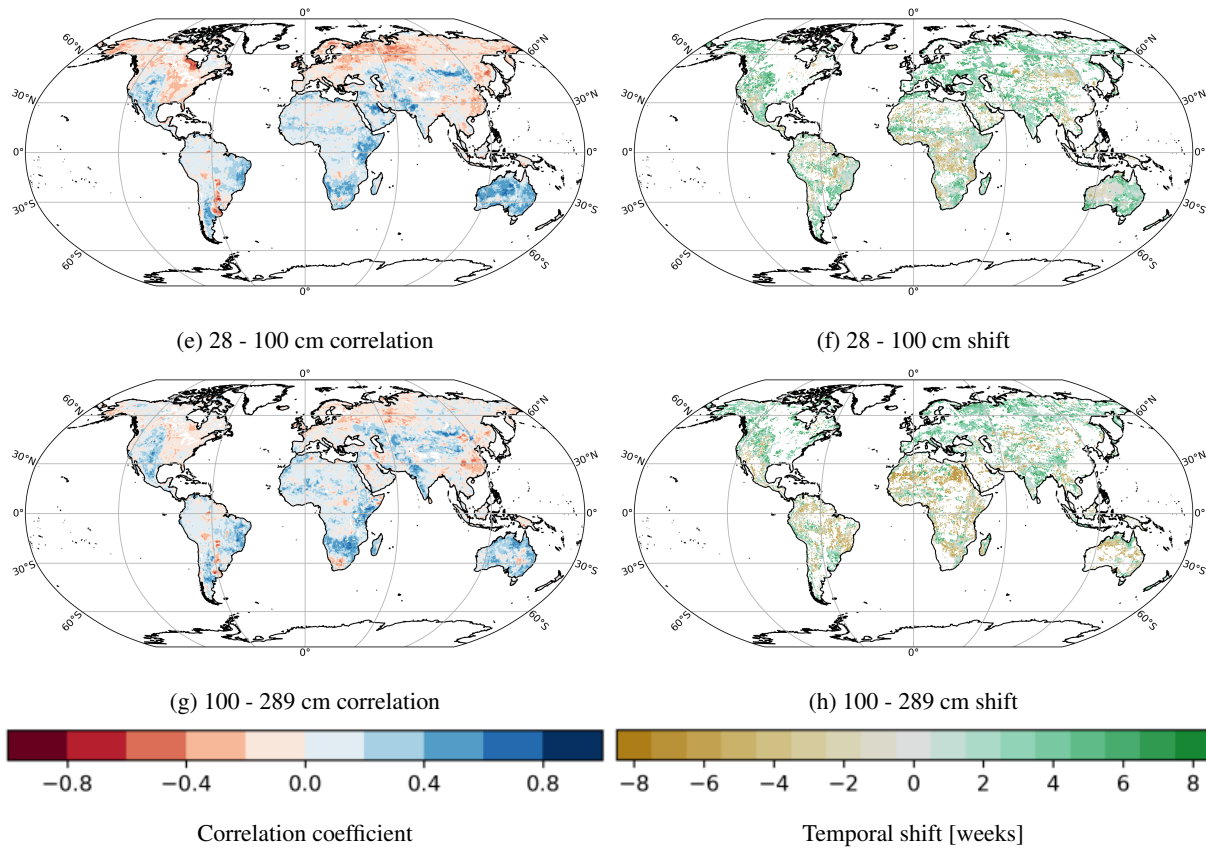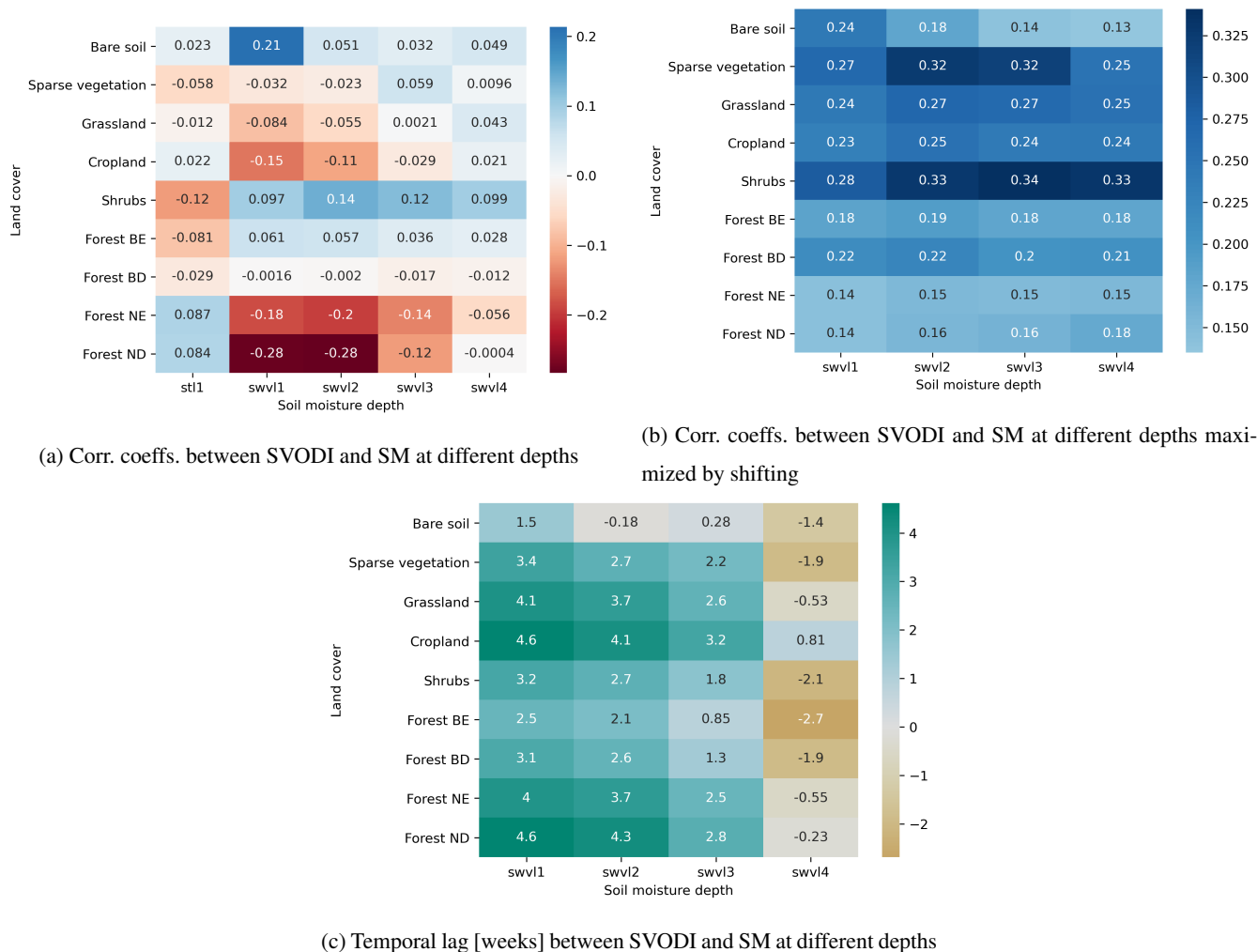
(e) 28 - 100 cm correlation

(f) 28 - 100 cm shift

(g) 100 - 289 cm correlation

(h) 100 - 289 cm shift

Correlation coefficient

Temporal shift [weeks]

Figure 8. Correlation (left column) and temporal shift (right column) between SVODI and soil moisture anomalies from ERA5, based on weekly data. Positive (green) values in the shift plots indicate that anomalies are earlier visible in soil moisture than in SVODI. (last part)

(a) Corr. coeffs. between SVODI and SM at different depths

(b) Corr. coeffs. between SVODI and SM at different depths maximized by shifting

(c) Temporal lag [weeks] between SVODI and SM at different depths

Figure 9. Mean correlation coefficient if no temporal shifting is done (a), maximum correlation obtained by temporal shifting (b) and the corresponding temporal shift in weeks between SVODI and soil moisture anomalies (c) at different ERA5 depths. The depths are: swvl1 0-7 cm, swvl2 7-28 cm, swvl3 28-100 cm, swvl4 100-289 cm. (a) also shows the correlation with the surface soil temperature, stl1.
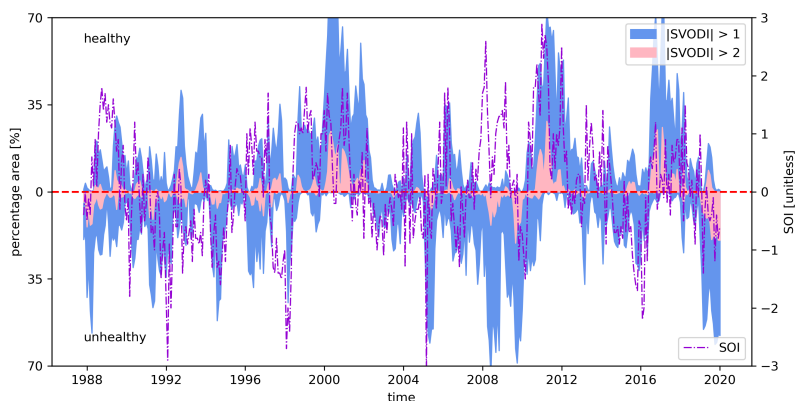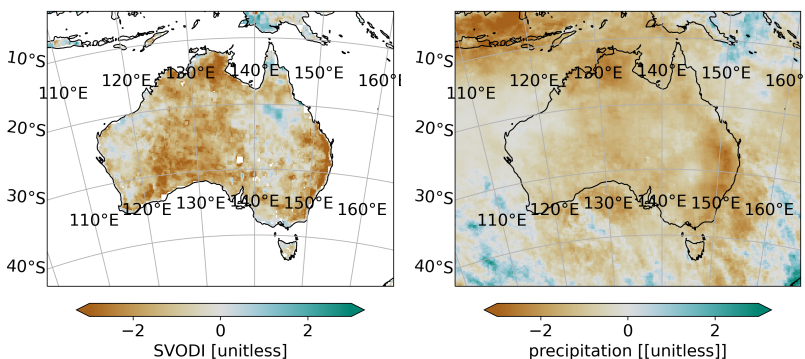
(a) SVODI extreme values over time and SOI
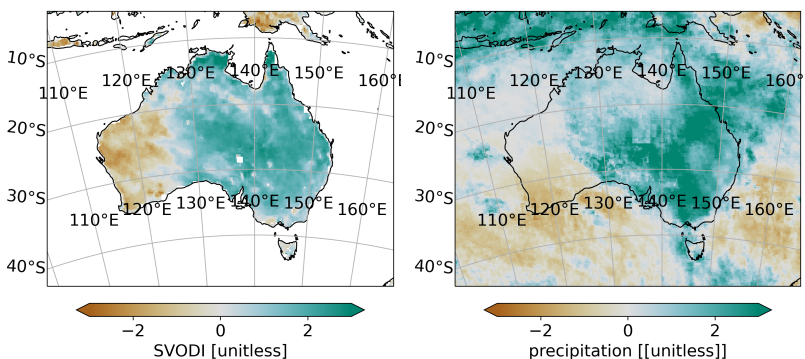
(b) SVODI 2010-11

(c) Precipitation 2010-11

(d) SVODI 2019-12

(e) Precipitation 2019-12

Figure 10. Fraction of Percentage area of SVODI greater/smaller than 1/-1 and 2/-2 respectively for central Australia together with the SOI (top), SVODI (left) and standardized precipitation anomalies (right) for 2010-11 and 2019-12.
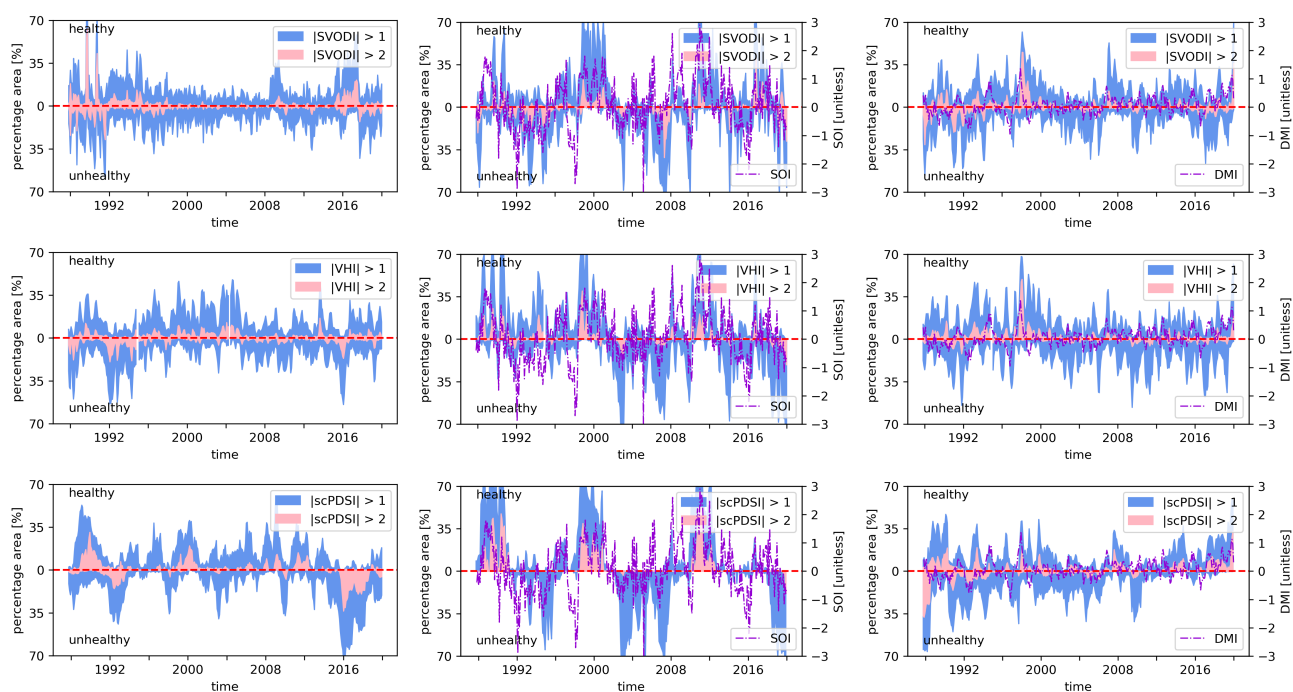
Figure 11. Percentage area of SVODI (top row), standardized VHI (center row) and scPDSI (bottom row) greater/smaller than 1/-1 and 2/-2 respectively for selected AR6 (Iturbide et al., 2020) regions. Left column: Northern South America, Center column: Eastern Australia, right column: North Eastern Africa. All datasets are downsampled to the monthly resolution of scPDSI.
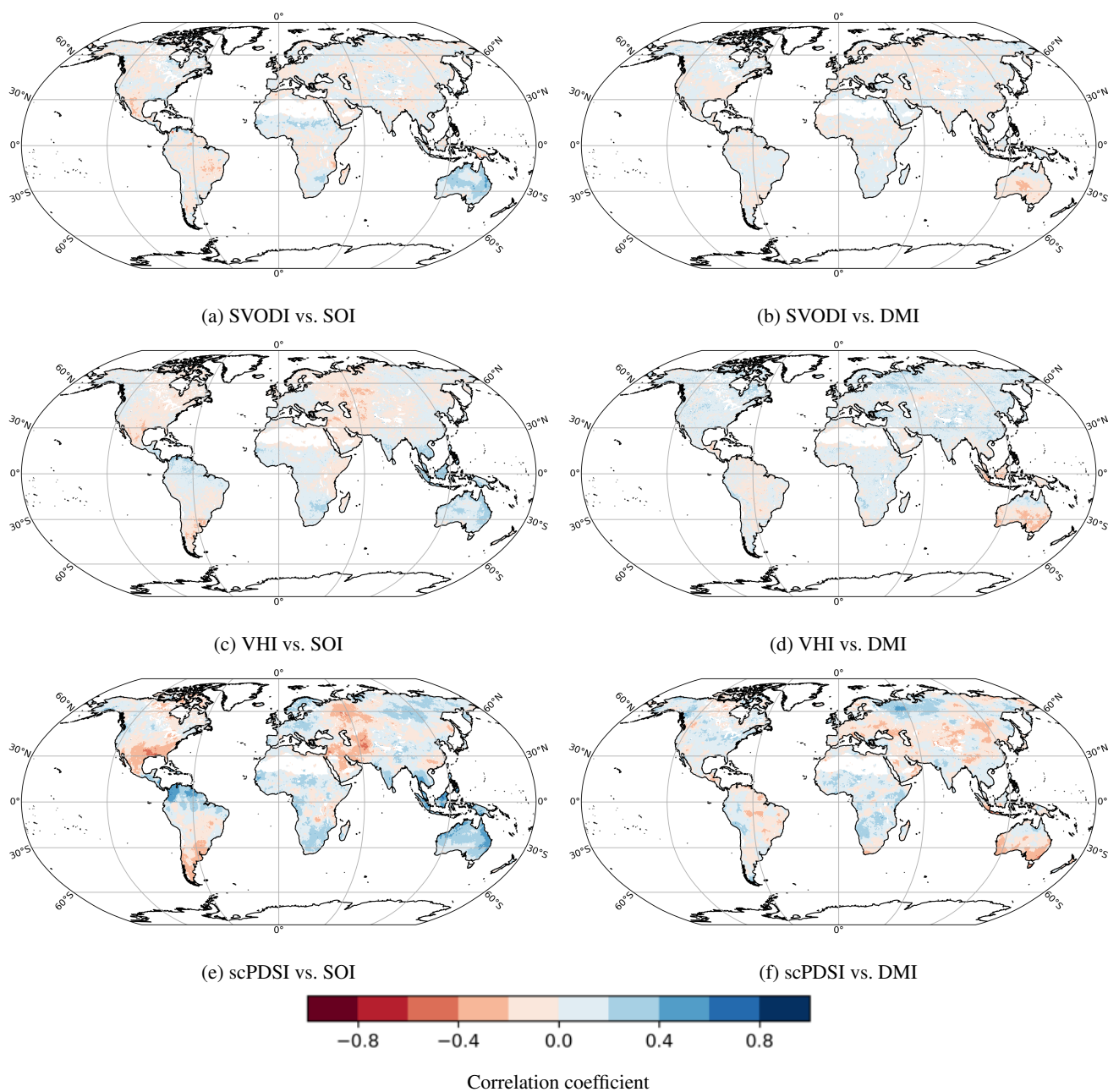
(a) SVODI vs. SOI

(b) SVODI vs. DMI

(c) VHI vs. SOI

(d) VHI vs. DMI

(e) scPDSI vs. SOI

(f) scPDSI vs. DMI

Correlation coefficient

Figure 12. Correlation coefficients between SVODI, VHI and scPDSI (top to bottom) vs. SOI (left column) and DMI (right column)